IEEE Access
Multidisciplinary ⋮ Rapid Review ⋮ Open Access Journal

Received November 2, 2021, accepted December 20, 2021, date of publication December 23, 2021,
date of current version January 4, 2022.

Digital Object Identifier 10.1109/ACCESS.2021.3137868

Electronic Structure and Thermoelectric Properties of Mg_2Sn Films Fabricated by Using Co-Sputtering Process With Stoichiometric Modification

SARA KIM AND NAM-HOON KIM
Department of Electrical Engineering, Chosun University, Gwangju 61452, South Korea

Corresponding author: Nam-Hoon Kim (nhkim@chosun.ac.kr)

This work was supported in part by the Gwangju Jeonnam Local Energy Cluster Manpower Training of the Korea Institute of Energy Technology Evaluation and Planning (KETEP) Grant through the Korea Government Ministry of Trade, Industry and Energy (MOTIE) under Grant 20214000000560; and in part by the KETEP Grant through the Korea Government (MOTIE) under Grant 20184010201650.

ABSTRACT Colossal values of the Seebeck coefficient were first discovered in Mg-poor Mg_2Sn films in the temperature range 600–700 K. Cubic and orthorhombic structures of the Mg_2Sn films for solid-state thermoelectric energy conversion devices were prepared by radio frequency (RF) magnetron co-sputtering. The Mg-Sn films showed a structural phase transition between the metastable orthorhombic and the stable cubic structures as the atomic ratio Mg/Sn varied near the stoichiometric ratio. The Mg-poor orthorhombic Mg-Sn films transited from p-type to n-type conductivity at 500 K and exhibited colossal values of the Seebeck coefficient and power factor in the temperature range 600–700 K. The colossal Seebeck coefficient, which exceeded -10 mVK^{-1}, indicates long-term stability over a wide temperature range. Furthermore, the energy band structure and density-of-state were calculated for the cubic and the orthorhombic Mg_2Sn using the first-principles calculation with the Perdew-Burke-Ernzerhof (PBE0) hybrid functionals, which yielded results that were consistent with the experimental data.

INDEX TERMS Mg_2Sn films, electronic structure, thermoelectric properties, stoichiometric modification, colossal Seebeck coefficient, sputtering.

I. INTRODUCTION

Thermoelectric (TE) materials are functional materials that can be used for direct and reversible conversion between waste heat and useful electrical power [1], [2]. Thermoelectric generators (TEGs) are solid-state energy converters with no moving parts, having a high power density, and an excellent long-term reliability. Moreover, they require little or no maintenance and potentially generate electrical energy in an environmentally friendly manner and independent of fossil fuels. The conversion efficiency of TE devices scales with the performance of the TE materials, which is quantified by the dimensionless TE figure of merit $ZT = S^2T/\rho\kappa$, where S, ρ, $S^2\rho$, T, and κ are the Seebeck coefficient, electrical resistivity, power factor (PF), absolute temperature, and the total thermal conductivity, respectively [3]. Bulk TE materials are used for power generation, because they can generate substantial amounts of converted energy; however, it is difficult to employ bulk materials in miniaturized electronic devices because of their large volume. To realize the potential of powering miniaturized devices through efficient thermal energy conversion by solid-state TE materials-based conversion devices, the TE materials must be produced in the form of films [4]–[6]. The highest values of ZT are usually achieved in compounds that contain rare or heavy-metal elements such as Te or Pb, which severely limits the widespread applications of TE materials because of ecological and economic considerations [7]. In recent years, $A_2^{IIA}B^{IV}$ compounds, which crystallize in a cubic antifluorite structure, have received considerable attention because of their fundamental and technological significance [8], [9]. In particular, Mg_2B^{IV} (B^{IV} = Si, Ge, Sn) semiconductor compounds offer a high thermal stability, low cost, low density, nontoxicity, constituent abundance, and environmental-friendliness, and

The associate editor coordinating the review of this manuscript and approving it for publication was Michail Kiziroglou.

This work is licensed under a Creative Commons Attribution 4.0 License. For more information, see https://creativecommons.org/licenses/by/4.0/

provide both n- and p-type conductivities [10]. These intermetallic compounds Mg_2B^{IV} (B^{IV} = Si, Ge, Sn), which are mixed ionic-covalent-semiconductors that crystallize in the cubic antifluorite structure, are promising TE materials for power generation [11], [12]. Among these TE compounds, Mg_2Sn is especially promising because it has a PF comparable to those of more conventional Bi_2Te_3 and $YbAl_3$ TE materials, but costs less than a quarter of their price [13]. However, the development of Mg_2Sn as a sustainable TE material is hindered by its difficult and time-consuming synthesis [14], [15], which is attributed to the high vapor pressure of Mg in the fabrication of Mg_2B^{IV} system. To compensate for the loss of Mg due to its high vapor pressure during synthesis, excess Mg up to 4 wt% was added to the stoichiometry in previous works [16]. Mg_2Sn-based TE compounds are mainly prepared by the casting and powder methods under controlled atmospheric conditions [17]–[20]. Several different methods have been suggested to produce TE films. These methods include flash evaporation, pulsed laser deposition (PLD), electrochemical deposition, metal organic chemical vapor deposition (MOCVD), molecular beam epitaxy (MBE), and sputtering [21]. Among these methods, sputtering has numerous advantages such as good reproducibility and control over the film composition and homogeneity. In this study, Mg_2Sn films are prepared by a co-sputtering method with Mg and Sn targets in consideration of the high vapor pressure and chemical reactivity of Mg. The stoichiometric compositions and co-sputtering process conditions are controlled to ensure the stability of the Mg_2Sn films and their TE properties.

II. EXPERIMENTAL DETAILS

Mg-Sn films were deposited on 2 × 2 cm^2 Corning glass substrates using an RF magnetron co-sputtering system (IDT Engineering Co., Korea) in which the sputtering power of the Sn (TASCO, Korea, 99.99% purity, 2-inch diameter) target was varied from 78 to 83 W and the sputtering power of the Mg (TASCO, Korea, 99.99% purity, 2-inch diameter) target was fixed at 90 W. The other parameters for co-sputtering were kept constant at the following values: The pre-sputtering time prior to each run was 3 min, the Ar gas flux was 20 sccm, the base pressure was 1.0×10^{-6} Torr, the substrate-to-target distance was 5.0 cm, and the vacuum pressure was 7.5×10^{-3} Torr during sputtering at room temperature. The thickness of the films deposited over the deposition time of 30 min estimated from a cross-sectional field emission scanning electron microscope (FESEM) images ranged from 1000 to 1200 nm. The crystalline structures of the films were analyzed using X-ray diffraction (XRD, PANalytical B.V., The Netherlands, X'pert-PRO-MRD, Cu Kα = 0.15405 nm, 40 kV, 30 mA). To examine the structural stability, a sample was subjected to rapid thermal annealing (RTA, GRT-100, GD-Tech Co., Korea) process at different temperatures up to 673 K for 1 hr under a N_2 gas atmosphere. The FESEM (S-4700, Hitachi, Japan, without Pt coating) was employed to reveal the morphological characteristics of the Mg-Sn films. An energy dispersive X-ray spectrometer (EDS) attached to the FESEM and X-ray photoelectron spectroscopy (XPS, Thermo Fisher Scientific Inc., USA, K-Alpha$^+$) were used to analyze the composition and chemical nature of the Mg-Sn films. Moreover, the electrical properties including the carrier concentration, resistivity, and mobility of the Mg-Sn films were characterized using a Hall effect measurement system (HL5500PC, Accent Optical Technologies, USA) at room temperature. The electrical resistivity (ρ) and the Seebeck coefficient (S) were simultaneously measured as a function of temperature up to 700 K using a modified commercial TE measurement system (TEP-800, Seepel Instrument, Korea). The Seebeck coefficient was measured by thermally connecting the two opposite sides of the sample to two different heaters at different temperatures, to create a temperature difference (ΔT). Further, the resulting potential difference (ΔV) was measured, and the Seebeck coefficient was calculated as the ratio of $\Delta V/\Delta T$. Each measurement cycle started at 300 K and the sample was heated up to 700 K with a ramp of 1 K min^{-1}. The PF was calculated using the experimental data of the Seebeck coefficient and the electrical resistivity. The measurement errors of the calculated PF were smaller than 10% for all the reported cases. Moreover, the electronic band structure and density-of-states (DOS) for the Mg_2Sn phases were studied using the density functional theory (DFT) framework implemented in the CAmbridge Serial Total Energy Package (CASTEP). First-principle calculations of the electronic structure of all Mg_2Sn phases were carried out with CASTEP19.0 using the Perdew-Burke-Ernzerhof (PBE0) hybrid functionals because these functionals provide more accurate values of the band gap for cubic Mg_2Sn compared to other functions. It is well known that the semiconductor band gaps are underestimated in the local-density approximation (LDA) and the generalized gradient approximation (GGA) framework, whereas hybrid functional calculations can provide more reliable band gap values that are consistent with experimental values. Besides, the experimentally determined unit cells were included in the geometry optimization for each composition, and the convergence tolerance parameters for the geometry optimization were set to an energy of 1×10^{-5} eV per atom, a maximum force of 0.03 eV/Å, a maximum stress of 0.05 GPa and a maximum displacement of 1×10^{-4} nm. The energy cutoff was set to 500 eV with norm-conserving pseudopotentials and the 4 × 1 × 3 k-point meshes for the Brillouin zone sampling were constructed using the Monkhorst-Pack scheme. The calculations were based on the experimental crystal structure data after refinement.

III. RESULTS AND DISCUSSION

The FESEM of the surface morphologies of the Mg-Sn films obtained at different Sn target sputtering powers are shown in Fig. 1. All the as-deposited Mg-Sn films cover the substrate surfaces perfectly without cracks or delamination. The main features in all the FESEM micrographs are the flower-like microstructures composed of several grains, which resulted

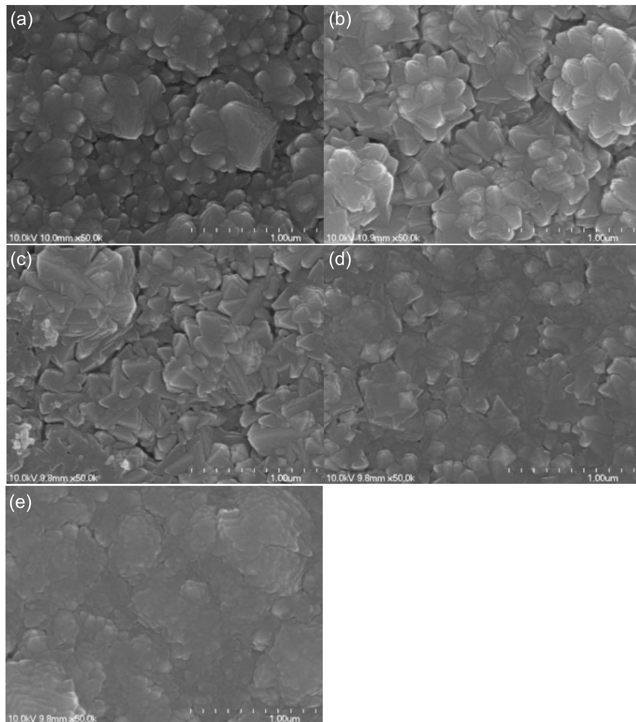

FIGURE 1. **Surface field emission scanning electron microscope (FESEM) images of the as-deposited Mg-Sn films fabricated by co-sputtering at the Sn sputtering powers of (a) 73, (b) 75, (c) 78, (d) 80, and (e) 83 W and the fixed Mg sputtering power of 90 W.**

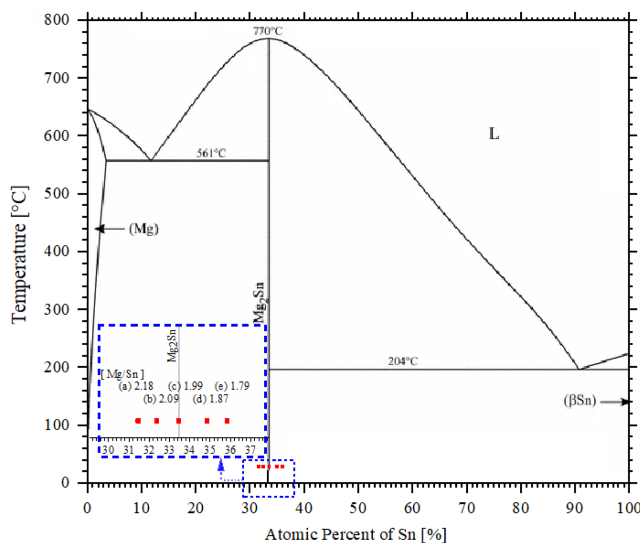

FIGURE 2. **Phase diagram of Mg-Sn binary system with the Mg/Sn atomic ratio of the Mg-Sn films under the same conditions [22], [23].**

from the extensive surface diffusion in the Mg-Sn films [24]. Further, these images clearly show that the Mg-Sn films have uniform microstructures with very fine and dense particles regardless of the Sn power and are made of large particles with lateral sizes around 1 μm as deduced from the FESEM images. The Mg-Sn films fabricated at low Sn power exhibited larger coalescence, as shown in Fig. 1(a)–(c). In addition, as the Sn target sputtering power increases, the morphology of the Mg-Sn films changes. At higher Sn powers, the Mg-Sn films exhibit smaller particles and dense and smooth surfaces, as shown in Figs. 1(d) and (e), owing to the larger amount of Sn in the films [25]. The Mg-Sn phase diagram corresponds to that of a classical two-eutectic congruently melting line-compound system [26]; any deviation from the 2/1 atomic ratio would therefore result in the presence of Sn- or Mg-free metal. The Mg_2Sn phases are known to be slightly reactive to oxygen and highly reactive to water; therefore, there might be oxide layer growth at the surface of the particles [26], [27]. Elemental analysis of the Mg-Sn films was carried out through EDS measurements. Figure 2 shows the atomic ratio of Mg/Sn in the Mg-Sn films for each Sn sputtering power. The results show that the Mg/Sn ratio in the elemental composition of these Mg-Sn films exhibits a linear decrease from Mg/Sn = 2.18 to Mg/Sn = 1.79, as the Sn power increases. The Mg/Sn atomic ratios at the Sn powers of 73, 75, 78, 80, and 83W were 2.18, 2.09, 1.99, 1.87, and 1.79, respectively. The sputtering powers for the Sn target were designed to deviate toward Mg-rich and Mg-poor compositions from almost-stoichiometric Mg_2Sn at the Sn sputtering power of 78 W. The EDS results show that the Mg-Sn films are Mg-rich for the Sn sputtering powers of 73 and 75 W, while the films are Mg-poor at the Sn sputtering powers of 80 and 83 W.

Figure 3 shows the XRD patterns of the as-eposited Mg-Sn films with various sputtering powers of the Sn target at room temperature. The XRD patterns of the Mg-rich films sputtered at the Sn sputtering powers of 73 and 75 W indicate a well-crystallized cubic Mg_2Sn phase (stable form, JCPDS No. 07-0274), as shown in Fig. 3(a) and (b). The XRD patterns of the Mg-rich films show two main peaks at $2\theta = 22.7°$ and 37.4°, which are indexed to the (111) and (220) planes of cubic Mg_2Sn, respectively. Although Mg-rich films contain excess Mg, Mg-related hexagonal peaks are absent from the XRD results. This indicates that the excess Mg might be in a non-crystalline form and/or it is present in very little amount in the Mg-Sn films. Small diffraction peaks are observed at $2\theta = 44.2°$, 59.3°, and 67.3°, which correspond to the (311), (331), and (422) preferred orientations (JCPDS No. 07-0274), respectively. The evolution of the width and peak positions in the XRD patterns at larger Sn sputtering powers reveal the onset of phase transitions in the Mg-Sn films. As shown in Fig. 3(c), the most intense peak at $2\theta = 22.7°$, which corresponds to the (111) plane of the cubic Mg_2Sn phase, starts to decrease as the Sn sputtering power increases. This indicates that there is a phase transformation from the cubic structure to a mixed structure of the cubic Mg_2Sn and metastable orthorhombic Mg_2Sn phases [21]. As the Sn sputtering power increases further to 80 W, a phase transition into a pure orthorhombic Mg_2Sn phase (JCPDS No. 31-0812) and a secondary Sn phase occurs, as indicated by XRD patterns in Fig. 3(d). This transformation from the cubic to the orthorhombic phases is similar to what was previously observed in the binary Mg-Sn system [21], [28]. Because the formation of non-stoichiometric Mg_2Sn is not expected from the phase diagram, the excess Sn should remain at the grain

boundaries or on the surface [24], [29], [30]. The metallic Sn peaks increase along with the body-centered tetragonal phase, as indicated by the distinctive diffraction peaks at $2\theta = 30.64°$ and $32.05°$, that correspond to the (200) and (101) crystal planes, respectively, as shown in Fig. 3(c)–(e). The orthorhombic Mg_2Sn phase is confirmed by the five major peaks at $2\theta = 23.10°$, $24.02°$, $33.66°$, $40.80°$, and $41.34°$, which are indexed to the (400), (221), (422), (125), and (523) planes, respectively, and the small diffraction peaks at 35.9°, 47.50° and 64.20°. It is inferred that high Sn content in the Mg-Sn films may not result in phase transitions, and must be accompanied by sufficient sputtering power to transfer the formation energy to Mg_2Sn, because the orthorhombic Mg_2Sn has a larger formation energy than the cubic Mg_2Sn. In general, the transition pressure is the pressure at which the enthalpies of the two phases are equal, and the most stable phase corresponds to the phase with the minimum energy [31]. The phase transitions in this study occur because the sputtering powers used are designed to be large enough to encompass this transition point without applying additional annealing treatment or external pressure.

To identify the element bonding in the Mg-Sn films, XPS analysis was performed on the films with the Sn sputtering powers of 73, 78, and 83 W. These three Sn sputtering powers were determined by the EDS/XRD analysis of the resultant Mg-Sn films corresponding to the representative conditions of the Mg-rich/cubic, stoichiometric/mixture (transition), and Mg-poor/orthorhombic phases, respectively. The spectrum of the C 1*s* peak at the binding energy of 285 eV was used as a reference for data calibration. All XPS spectra were deconvoluted using the XPSPEAK4.1 software. High-resolution narrow scans were employed to examine the core level elements, such as Mg 1*s*, Mg 2*p*, and Sn 3*d*, in the Mg-Sn films. The cubic Mg_2Sn has an anti-fluorite crystal structure (No.255, space group is Fm3m, and the lattice constant of 0.676 nm), which consists of interpenetrating fcc cubic lattices with Sn^{4+} at the origin (0, 0, 0) and Mg^{2+} at the ± (1/4, 1/4, 1/4) position [27], [32]. In addition, the coordination number of each Sn ion is 8, while each Mg ion is located in the middle of the Sn^{4+} tetrahedral crystal structure [26]. Therefore, the cubic Mg_2Sn phase can be described as a compact fcc lattice network of Sn atoms with all the tetrahedral sites occupied by eight Mg atoms [26], [33]. The XPS Mg 1*s* peak is exhibited in the three Mg-Sn films with the Sn sputtering powers of 73, 78, and 83 W, as shown in Fig. 4(a), (d), and (g), respectively. A noticeable Mg 1*s* peak at the binding energy of approximately 1304.20 eV, which corresponds to Mg bonded to Sn in the Mg-Sn films as reported for Mg_2Sn [24], is present in the spectra for all the Sn sputtering powers; no superposition of other peaks is observed in the deconvolution result of the Mg 1*s* peaks. For the Mg 2*p* peaks shown in Fig. 4(b), (e), and (h), all the Mg-Sn films comprise two components with binding energies of approximately 50.9 eV and 49.7 eV, which are attributed to Mg_2Sn and elemental Mg, respectively. At the Sn sputtering power of 83 W, the elemental Mg component is shifted to higher binding energy of 50.3 eV [34], as shown in

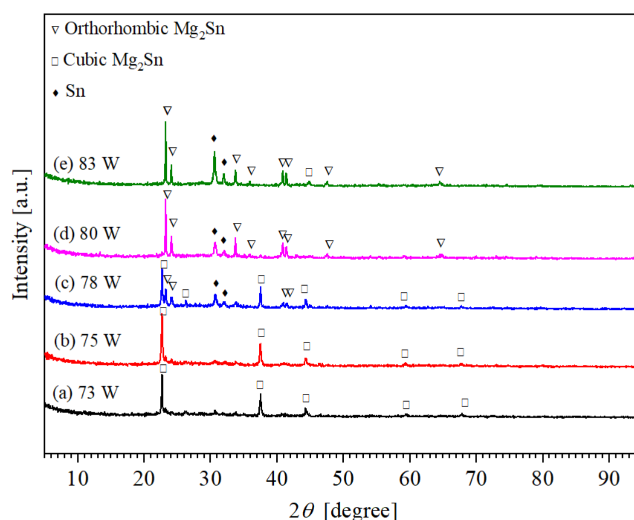

FIGURE 3. X-ray diffraction (XRD) patterns of the as-deposited Mg-Sn films fabricated by co-sputtering at the Sn sputtering powers of 73, 75, 78, 80, and 83 W and the fixed Mg sputtering power of 90 W.

Fig. 4(h), because Mg becomes more electropositive as more elemental Mg is bonded with Sn at higher Sn sputtering powers. The area ratio of the elemental Mg component decreases gradually from approximately 36% at 73 W to 33% at 78 W and then to approximately 28% at 83 W, as the Sn sputtering power and content increase.

The Sn 3*d* doublet spectrum is symmetric and narrow and comprises the two split peaks of Sn $3d_{5/2}$ and Sn $3d_{3/2}$ at 484.60–485.00 eV and 493.15 eV, respectively [24], [35]. As exhibited in Fig. 4(c), (f), and (i), the deconvolution of the Sn $3d_{5/2}$ peak reveals several components that correspond to SnO_2, Mg_2Sn, and elemental Sn. The binding energy of elemental Sn is approximately 484.9 eV, which can be observed from the XPS spectra of the stoichiometric film and the Mg-poor Mg-Sn films at 78 and 83 W, respectively; however, there is no elemental Sn component in the XPS spectrum of the Mg-rich Mg-Sn film at 73 W, which is consistent with the XRD pattern (Fig. 3). Because Sn tends to gain electrons in the Mg_2Sn lattice, the binding energy in the Mg_2Sn lattice is reduced compared to that of elemental Sn [24]. The specific component of Sn $3d_{5/2}$ at 483.9 eV in the XPS pattern is assigned to Mg bonded to Sn in the Mg_2Sn lattice [36], [37]. There is a shoulder that corresponds to SnO_2, which is located at higher binding energies of approximately 470 eV. The SnO_2 component in the XPS Sn 3*d* spectra is believed to be due to easy oxidation of the Sn metal on the surface during the *ex-situ* XPS analysis, which occurs even at normal temperature. A 0.5 eV shift of the binding energy is observed in the Mg-Sn film with the Sn sputtering power of 78 W, which consists of both cubic and orthorhombic Mg_2Sn phases. This chemical shift towards higher binding energy without any obvious change in the spectral shape is due to the large electronegativity difference between the coordinating groups. This difference can be attributed to the formation of a large number of crystal defects at the transition point from the

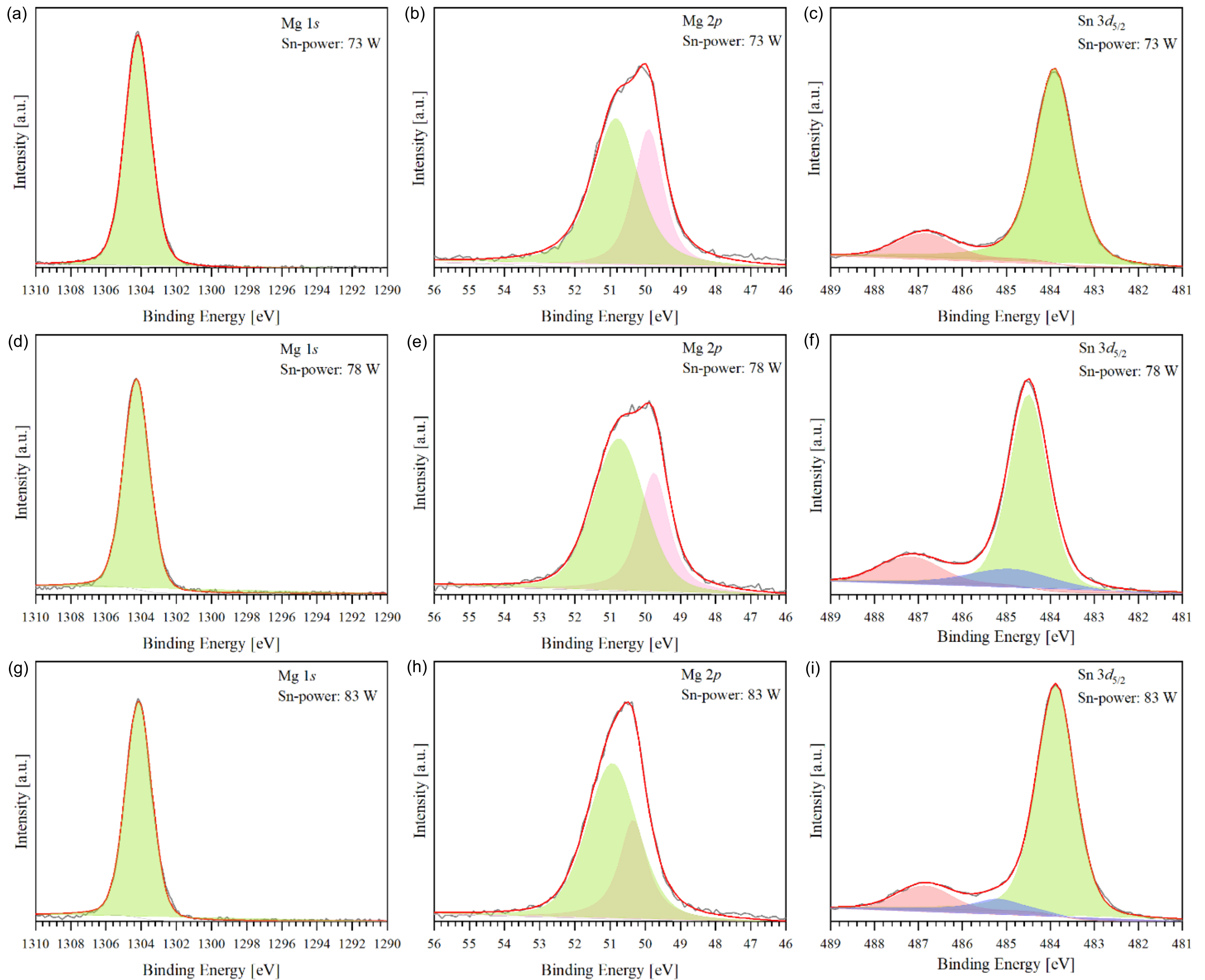

FIGURE 4. X-ray photoelectron spectra of (a,d,g) Mg 1*s*, (b,e,h) Mg 2*p*, and (c,f,i) Sn $3d_{5/2}$ obtained from the as-deposited Mg-Sn films fabricated by co-sputtering at the Sn sputtering powers of (a,b,c) 73, (d,e,f) 78, and (g,h,i) 83 W and the fixed Mg sputtering power of 90 W.

cubic to the orthorhombic phases [38]. This chemical shift can also be attributed to the change in the band gap at the phase transition, which shifts both the Fermi energy (E_F) and the entire XPS spectra [39], [40].

As observed from the XRD results, there is a transformation from the cubic to the orthorhombic structure at high Sn sputtering power. Internal pressure is the governing force behind the phase transition in this study [41], [42], because the transition can be induced by either increasing the pressure at a constant temperature or by increasing the temperature at a finite pressure [41]. The transition is a reconstructive first-order transition and involves the formation of several crystalline defects in Mg_2Sn films, which can result in a change of conduction by the Mg vacancies as the Sn content increases [41], [43], [44]. Additionally, the phase transition is readily initiated by enhanced defect incorporation and mechanical deformation [36]. Random local field defects are especially important for first-order phase transitions between phases with different symmetries [44], [45]. Depending on the symmetry of such defects, the structure can be stimulated to transit to either a higher or lower degree of symmetry. In other words, the phase transition temperature can either increase or decrease depending on the symmetry of the defects [44], [46]. The difference in the local concentration of such defects can result in the occurrence of phase transition, at different temperatures and at different spatial locations, in the Mg-Sn films [44].

The electrical properties, comprising the resistivity (ρ), carrier mobility (μ), and carrier concentration (n) of the Mg-Sn films were analyzed by Hall effect measurements at room temperature. All the Mg-Sn films exhibit p-type conductivity regardless of the sputtering power of the Sn target with carrier concentrations between 7×10^{19} and 5×10^{20} cm^{-3}, as shown in Fig. 5. For the Mg-rich films with

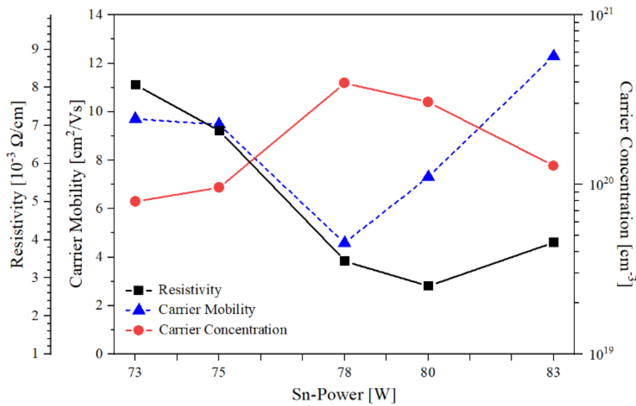

FIGURE 5. Electrical resistivity (ρ), carrier mobility (μ), and carrier concentration (n) of the Mg-Sn films obtained from Hall effect measurements at room temperature at the Sn sputtering powers of 73, 75, 78, 80, and 83 W and the fixed Mg sputtering power of 90 W.

the Sn sputtering powers of 73 and 75 W, the obtained carrier concentrations are less than the optimal carrier concentration 10^{20} cm^{-3} for TE applications [47].

The experimental results also show that Mg-rich conditions result in carrier concentrations on the order of 10^{19} cm^{-3}, which are less than the optimal values required to maximize the power factor. Besides, there is an increase in the carrier concentration as the Sn sputtering power increases to 78 W (i.e., from Mg-rich to stoichiometric conditions). Mg vacancies (V_{Mg}) and interstitial Mg (Mg_I) are deduced to be the main defects in Mg_2Sn compounds because of their relatively low formation energies; therefore, their concentration determines the intrinsic conductivity of Mg_2Sn compounds [33], [47], [48]; while V_{Mg} and Mg_I behave as acceptor and donor sites, respectively. The p-type conductivity of Mg-Sn films in this study indicates a higher concentration of V_{Mg} compared to Mg_I [43], [49]. The increase in the carrier concentration in Mg-Sn films with Sn sputtering power can be explained by the formation of V_{Mg}^{2-} with holes ($2h^+$). As the atomic ratio of Mg/Sn increases under Mg-rich conditions, the probability of forming the Mg-deficient Mg_2Sn phase is lower because of the excess Mg atoms, which results in a lower carrier concentration in the Mg-Sn film sputtered with Sn at 73 W. It can be observed that the Mg-Sn film still exhibit p-type conductivity even in this extreme Mg-rich condition. Such persistent behavior is a characteristic of an intrinsic killer defect that causes pinning of the E_F [43], [49]. The Mg-Sn film with the Sn sputtering power of 78 W, which was shown by XRD analysis to have transformed from the cubic to the orthorhombic phase, shows the highest carrier concentration and lowest carrier mobility among all the Mg-Sn films; also, it has the largest defects, as described earlier in the discussion on the XPS analysis. The defects scatter free carriers efficiently, thereby reducing their lifetime and carrier mobility [50]. Jiang *et al.* observed that interstitial and vacancy defects reduce the electron mobility significantly while antisite defects have a relatively smaller effect [51]. The abrupt change in carrier concentration and carrier mobility coincides with the structural phase transition, which strongly indicates that the crystal structure, carrier concentration, defect, and carrier lifetime are intrinsically correlated to one another [52]. As the Sn sputtering power increases to 80 W, the carrier concentration decreases, which can be explained by Sn substitution in the Mg sites (Sn_{Mg}^{+}) [33], [43], [47]. Although the Mg vacancies (V_{Mg}^{2-}) are the dominant defects and act as shallow acceptors in Mg_2Sn compounds, the compensation of many free hole carriers by the Sn_{Mg}^{+} leads to a lower carrier concentration. In addition, when the Sn sputtering power is further increased to 83 W, the increase in Sn_{Mg}^{+} causes the carrier concentration to further decrease to a near-optimal value (10^{20} cm^{-3}). The resistivity of the Mg-Sn films depends mainly on the carrier concentration and mobility and is given by $\rho = 1/nq\mu$, where n, q, and μ represent the carrier concentration, the unit carrier charge, and the carrier mobility, respectively. The calculated resistivity is in accord with the experimental results, as shown in Fig. 5.

To further understand the different behaviors of the Mg-rich and Mg-poor Mg-Sn films, DFT calculations were performed to determine the electronic structures of the cubic and orthorhombic phases of Mg_2Sn. The Seebeck coefficient is a parameter that depends on the electronic structure near E_F, which is in turn sensitive to other parameters such as the effective mass, carrier concentration, and band shape. The Seebeck coefficient is inversely proportional to the carrier concentration, as shown in Eq. (1):

$$S = \frac{8\pi^2 k_B^2 T}{3qh^2} m_d^* \left(\frac{\pi}{3n}\right)^{2/3}, \quad (1)$$

where S is the Seebeck coefficient, k_B Boltzmann's constant, T the absolute temperature, q the carrier charge, h Planck's constant, m_d^* the effective mass, and n the carrier concentration. The electronic and band structures of semiconductors play a crucial role in determining the charge carriers; also, the TE properties are quite sensitive to the details of the band structure. The band gap is a critical parameter for TE transport, particularly at higher temperatures, at which thermal energy can overcome the band gap energy of the materials. Using PBE0 implemented in the CASTEP package, the first-principles band structures of Mg_2Sn were calculated over a wide energy range. For clarity, the energy dispersion curves for the cubic and orthorhombic structures only show energy values from −5.0 to 5.0 eV and from -2.0 to 2.0 eV, respectively, as represented in Fig. 6. The band structure indicates that the cubic structure is indirect semiconductor. The valence band maximum (VBM) is located at the Γ point, and the conduction band minimum (CBM) at the X point in the cubic Mg_2Sn phase, as shown in Fig. 6(a). The band structure of cubic Mg_2Sn has a narrow band gap of approximately 0.413 eV, which is somewhat larger than the experimental values; a similar result with a value of approximately 0.460 eV has been reported in a previous study [53]. However, the orthorhombic Mg_2Sn phase does not have a clear band structure, as shown in Fig. 6(c) and the conduction and valence bands overlaps. The phase transition occurs together with

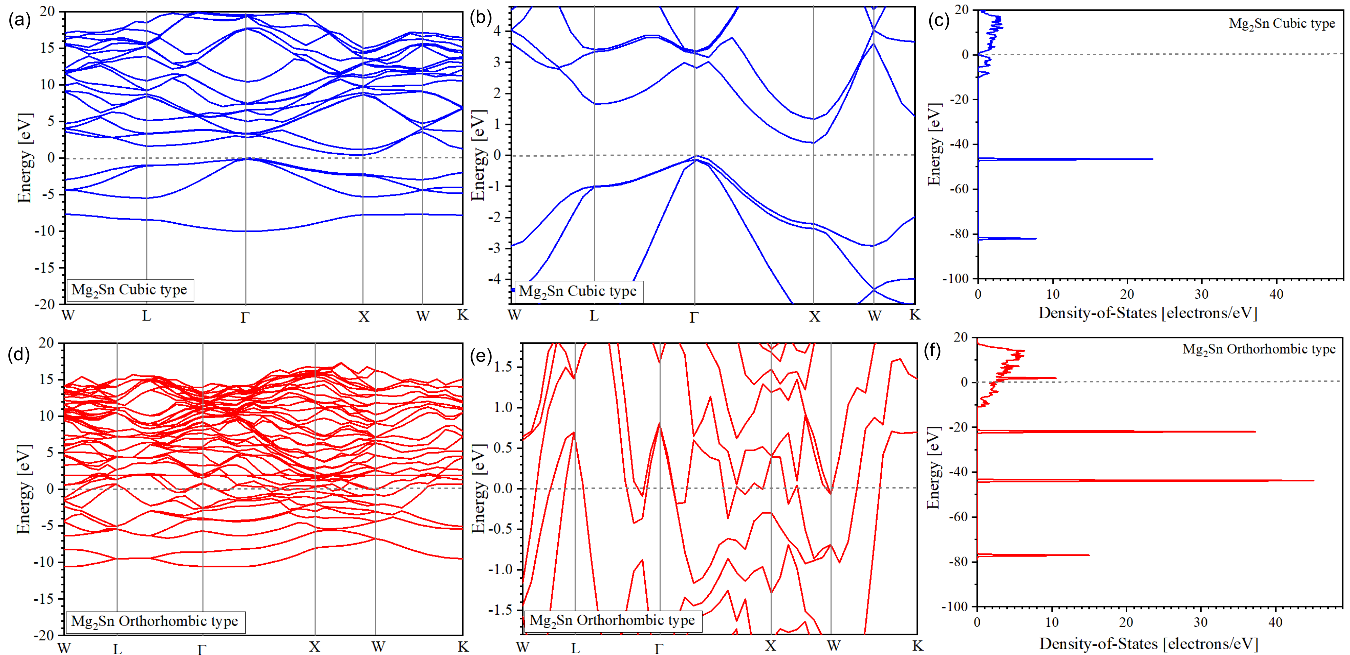

FIGURE 6. (a,d) Density functional theory (DFT) band structure, (b,e) a magnified view of the band structure near the Fermi level, and (c,f) total density-of-states (DOS) of the (a,b,c) cubic type and (d,e,f) orthorhombic type structures of Mg_2Sn.

an electronic bandgap collapse [54], [55]. This significant change in the band structure is due to the induced pressure which results in a structural phase transition in the Mg_2Sn lattice because of significant atomic and electronic structure modification [56]. The relatively large shift in the valence band is common feature in semiconductors undergoing phase transitions [39]. A multi-valley type character is observed in the orthorhombic type band structure, showing several bands crossing the Fermi level which result in complex fermi surface [57]. Different temperature dependence of multi-valleys might lead to valley convergence, which results in increasing valley degeneracy and enhanced PF [58]. Figures 6(c) and (f) present the DOS of the cubic and orthorhombic structures of Mg_2Sn as a function of energy. Fermi level at 0 eV is represented by the horizontal dashed line. For the orthorhombic type, the intrusion of a conduction band is observed toward the valence band. The band gap has disappeared and a relatively large DOS value is seen at Fermi level. Since the E_F of the orthorhombic structure falls on a sharp peak, a small shift in the E_F will give a large variation in the carrier density at the Fermi level. As a result, this configuration can be expected to be unstable [59], [60], [54].

To investigate the instability of the orthorhombic structure discussed above, after sputtering deposition, an Mg- poor orthorhombic sample with an Mg/Sn ratio of 1.87 was selected and subjected to an RTA process at 373, 473, 573 and 673 K for 1 hour under a N_2 gas atmosphere. Fig.7 shows the XRD analysis of the as-eposited and annealed Mg-Sn films. It is noticeable that the film structure starts changing at the annealing temperature of 473 K and a small diffraction peak starts to appear at 2θ =22.7° which is indexed to

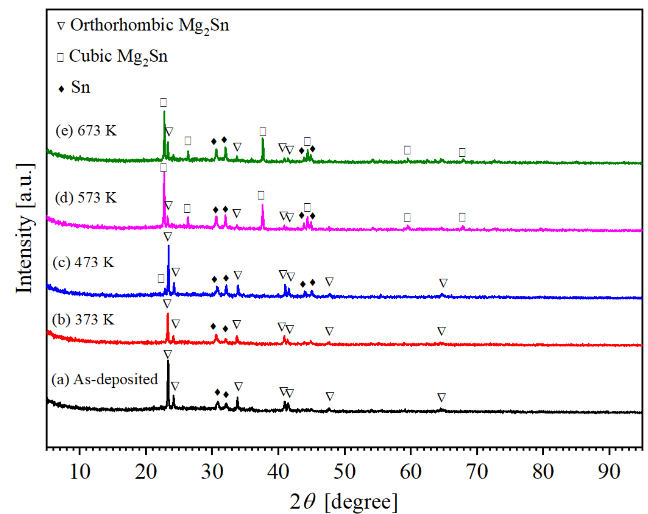

FIGURE 7. XRD patterns of the as-deposited and annealed Mg-poor orthorhombic Mg-Sn films with different annealing temperatures of 373, 473, 573, and 673 K.

the (111) plane of cubic Mg_2Sn. At annealing temperatures of 573 and 673 K, the most intense peak of orthorhombic structure at $2\theta = 23.10°$, which is indexed to the (400) plane of the orthorhombic Mg_2Sn phase, starts to decrease; and the cubic Mg_2Sn phase is confirmed by the four major peaks at $2\theta = 22.8°$, 26.2°, 37.7° and 44.3°. It is clear that at high temperatures, orthorhombic Mg_2Sn phase is decomposed to cubic Mg_2Sn and Sn phases as shown in Fig. 7.

The electrical resistivity and Seebeck coefficient of the Mg-Sn films were simultaneously measured as functions of

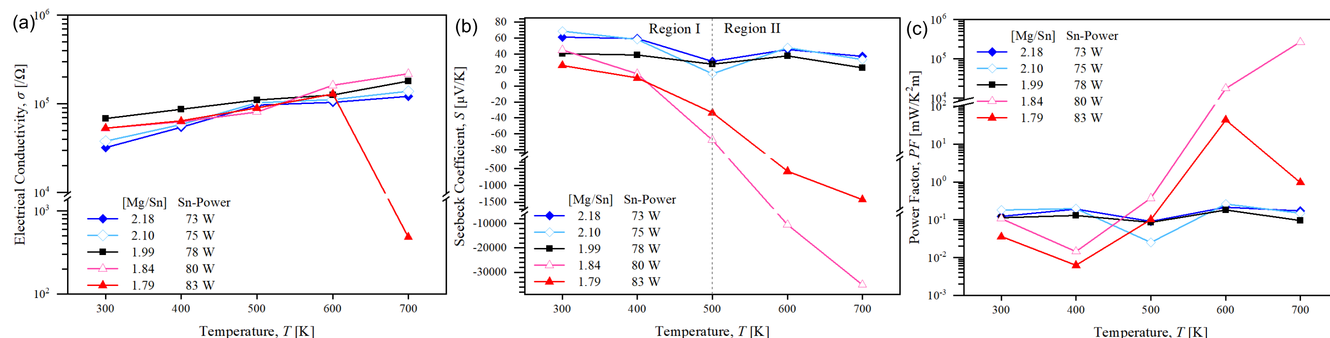

FIGURE 8. **Temperature dependence of thermoelectric properties: (a) conductivity, (b) Seebeck coefficient, and (c) PF of the Mg-Sn films with the Sn sputtering powers of 73, 75, 78, 80, and 83 W and the fixed Mg sputtering power of 90 W.**

the temperature over the range 300–700 K. The electrical conductivity, σ, of the Mg-Sn films exhibits an increasing trend with an increase in temperature, as plotted in Fig. 8(a), indicating that the Mg-Sn films exhibit a semiconducting behavior. The electrical conductivity of the Mg-Sn film with the Sn sputtering power of 83 W (i.e., Mg/Sn atomic ratio of 1.79) increases with temperature from 300 to 600 K and then decreases abruptly at 700 K. As observed from Fig. 7, Mg-poor films go through phase transition and this sharp drop in the electrical conductivity is attributed to the film that has gone through a complete transition. The electrical characteristics of the film will stabilize as the temperature increases further [61]. This transition is usually a gradual process that takes longer time than required to measure the Seebeck coefficient. Fig. 8(b) shows the temperature dependence of the Seebeck coefficient of the various Mg-Sn films. Both Mg-rich Mg-Sn films with the Sn sputtering powers of 73 and 75 W exhibit positive Seebeck coefficients corresponding to p-type conductivity in the temperature range of 300–700 K. The Seebeck coefficient is larger and positive for temperatures up to 400 K (Region I), signifying extrinsic conductivity, and then decreases as the temperature is further increased to 500 K, when the p-type carriers are gradually compensated by thermally activated n-type carriers. The slight increase in the Seebeck coefficient at 600 K is believed to be due to the annealing-like effect as the temperature increases during the measurement. The Seebeck coefficient of the stoichiometric Mg-Sn film with the Sn sputtering power of 78 W, which shows the highest carrier concentration at room temperature in Fig. 5, is almost temperature independent, confirming the dominance of extrinsic conductivity over intrinsic behavior. The Mg-poor Mg-Sn films with the Sn sputtering powers of 80 and 83 W show positive Seebeck coefficients for temperatures up to 400 K, and then a transition to intrinsic n-type conductivity occurs at temperatures higher than 500 K. In summary, as shown in Fig. 8(b), the Seebeck coefficient decreases with the compensation of extrinsic carriers by intrinsic carriers at increasing temperatures; with a further increase in temperature, its sign changes to that of an intrinsic behavior. Region II indicates the onset of intrinsic conductivity in the Mg-poor film. In this region, the number of thermally activated carriers exceeds the number of ionized impurity carriers. The transition from p- to n-type conductivity can also be attributed to the Sn segregation as the orthorhombic structure is decomposed to cubic Mg_2Sn and Sn phases in high temperature. The Sn-filled compounds exhibit n-type semiconducting behavior showing that Sn acts as an electron donor [62].

The Seebeck coefficient of the Mg-Sn films with the Sn sputtering powers of 80 and 83 W at 600 and 700 K, respectively, showed very unusual and surprisingly large values at about 10 times those of the previously reported values (Tables A1 and A2). The reproducibility of the colossal values of the Seebeck coefficient was verified several times through repeated analyses with different samples: Similar results were obtained as listed in the supplementary material (Tables A3 and A4). Clues to this phenomenon can be found in other TE materials. Kumar *et al.* correlated this strange Seebeck value to the phonon-drag phenomenon, in which a thermally induced flow of phonons pulls electrons along its way, leading to a large amplification of the Seebeck coefficient [63]. Battiato *et al.* identified the giant Seebeck coefficient mechanism in $FeSb_2$ as phonon-drag effect associated with an in-gap density of states [64]. Byeon *et al.* discovered colossal Seebeck in metallic Cu_2Se at the phase transition from low to high temperature phase and they showed that this phenomenon is because of the presence of a two-phase region where the low and high temperature phases coexist together in a stable condition [61]. As demonstrated in several nanocomposites based on PbTe [65], the formation of decomposed metallic Sn is also convinced to play a vital role in improving the Seebeck coefficient by enabling the energy barrier scattering. This unusually large Seebeck coefficient can be observed in semiconducting materials undergoing a structural transition. The first discovered colossal Seebeck coefficient of Mg_2Sn in this study was demonstrated to be related to the instability of the orthorhombic structure and its consecutive decomposition and transformation in high temperature; however, the source of this large Seebeck coefficient is not entirely understood, so more thorough research is required to understand the origin of this behavior. It can be observed that this large value of the Seebeck coefficient in

Mg_2Sn is stable over a long period of time, which means that it can be utilized for TE applications. It is believed that the Seebeck coefficient will decrease after the crystal structure transition is completed; however, further research is needed. Furthermore, the temperature dependence of orthorhombic Mg_2Sn is typical of degenerate semiconductors. Complex or multiband systems show greater band degeneracy than single-band systems [66]. The larger Seebeck coefficient obtained in the orthorhombic structure is also attributed to the larger DOS effective mass due to the anisotropic band structure and degenerate band valley in the conduction band. The large variation in the Seebeck coefficient is attributed to the variation of DOS during decomposition of the orthorhombic structure to cubic and Sn phase.

The p-type power factor of Mg_2Sn is found to be smaller than that of the n-type power factor owing to smaller band degeneracy and lower p-doping efficiency compared to the n-type doping efficiency. On the other hand, the Mg-rich Mg-Sn films show a stronger temperature dependence of the Seebeck coefficient than the Mg-poor films. The weak temperature dependence of the Mg-poor films can be related to the critical value of the energy band gap and the complexity of the band structure, as discussed above. Using the results for the electrical resistivity and Seebeck coefficient, the power factor (PF) of all the Mg-Sn films can be calculated using Eq. (2).

$$PF = S^2\sigma, \tag{2}$$

where PF is the TE power factor, S is the Seebeck coefficient, σ is the electrical conductivity, and T is the absolute temperature. While the cubic phase Mg-Sn films with the Sn sputtering power of 75 W showed a maximum PF of 0.260 mW/K^{2}m at 600 K, both orthorhombic Mg-poor Mg-Sn films exhibited colossal values of the power factor at 600 and 700 K because of the large Seebeck coefficient and high conductivity values discussed earlier.

IV. CONCLUSION

Cubic and orthorhombic near-stoichiometric Mg_2Sn films for TE applications with intentionally varied Mg/Sn atomic ratios were fabricated using RF magnetron co-sputtering by adjusting the sputtering power of the Sn and Mg targets. While the cubic Mg_2Sn films exhibited p-type conductivity regardless of the temperature, the orthorhombic Mg_2Sn films underwent a transition from p-type to n-type conductivity at 500 K. The orthorhombic Mg_2Sn films exhibited colossal values of the Seebeck coefficient and power factor, which can be utilized in TE applications in view of their long-term stability. This unusual behavior of Mg-poor films was attributed to the crystal instability of the orthorhombic Mg_2Sn films as observed by experiments and calculations. While the orthorhombic Mg_2Sn film outperformed the cubic Mg_2Sn film, the latter showed stronger stability across all the experimental temperature ranges. More detailed investigations are needed on the relationship and behaviors of the colossal Seebeck coefficient of Mg_2Sn with the crystal transition in subsequent studies.

ACKNOWLEDGMENT

The authors greatly appreciate the support of the facility for Seebeck coefficient measurements from Korea Institute of Machinery and Materials (KIMM), South Korea. They also thank Dr. Seungwoo Han for his advice in preparing the samples for measuring the Seebeck coefficient.

REFERENCES

[1] M. A. Zoui, S. Bentouba, J. G. Stocholm, and M. Bourouis, "A review on thermoelectric generators: Progress and applications," *Energies*, vol. 13, no. 14, p. 3606, Jul. 2020.

[2] Y. Zhang, "Thermoelectric advances to capture waste heat in automobiles," *ACS Energy Lett.*, vol. 3, no. 7, pp. 1523–1524, Jun. 2018.

[3] J.-I. Tani and H. Ishikawa, "Thermoelectric properties of Mg_2Sn thin films fabricated using radio frequency magnetron sputtering," *Thin Solid Films*, vol. 692, Dec. 2019, Art. no. 137601.

[4] W.-H. Chen, C.-Y. Liao, and C.-I. Hung, "A numerical study on the performance of miniature thermoelectric cooler affected by Thomson effect," *Appl. Energy*, vol. 89, no. 1, pp. 464–473, Jan. 2012.

[5] K. Yoshida, S. Tanaka, S. Tomonari, D. Satoh, and M. Esashi, "High-energy density miniature thermoelectric generator using catalytic combustion," *J. Microelectromech. Syst.*, vol. 15, no. 1, pp. 195–203, Feb. 2006.

[6] C. A. Gould, N. Y. A. Shammas, S. Grainger, and I. Taylor, "Thermoelectric cooling of microelectronic circuits and waste heat electrical power generation in a desktop personal computer," *Mater. Sci. Eng. B, Solid State Mater. Adv. Technol.*, vol. 176, no. 4, pp. 316–325, Mar. 2011.

[7] H. Kawamoto, "R&D trends in high efficiency thermoelectric conversion materials for waste heat recovery," *Quart. Rev.*, vol. 30, pp. 54–69, Jan. 2009.

[8] Q. Zhang, X. B. Zhao, T. J. Zhu, and J. P. Tu, "*Ab-initio* thermodynamic calculations of Mg_2B^{IV} (B^{IV} = Si, Ge, Sn) solid solutions," *Phys. Status Solidi, Rapid Res. Lett.*, vol. 2, no. 2, pp. 56–58, Mar. 2008.

[9] I.-H. Kim, "Mg_2B^{IV}: Narrow bandgap thermoelectric semiconductors," *J. Korean Phys. Soc.*, vol. 72, no. 10, pp. 1095–1109, May 2018.

[10] S. D. Guo, "Electronic structure and thermoelectric properties of $(Mg_2X)_2/(Mg_2Y)_2$ (X, Y = Si, Ge, Sn) superlattices from first-principle calculations," *Eur. Phys. J. B*, vol. 89, no. 5, pp. 1–5, May 2016.

[11] P. Pandit and S. P. Sanyal, "First principles study of electronic, elastic and lattice dynamical properties of Mg_2X (X = Si, Ge and Sn) compounds," *Indian J. Pure Appl. Phys.*, vol. 49, no. 10, pp. 692–697, Oct. 2011.

[12] G. Murtaza, A. Sajid, M. Rizwan, Y. Takagiwa, H. Khachai, M. Jibran, R. Khenata, and S. B. Omran, "First principles study of Mg_2X (X = Si, Ge, Sn, Pb): Elastic, optoelectronic and thermoelectric properties," *Mater. Sci. Semicond. Process.*, vol. 40, pp. 429–435, Dec. 2015.

[13] D. M. Rowe, "Thermoelectric waste heat recovery as a renewable energy source," *Int. J. Innov. Energy Syst. Power*, vol. 1, no. 1, pp. 13–23, Nov. 2006.

[14] S. C. Zhou, C. G. Bai, and C. L. Fu, "A fast synthesis and sintering of $Mg_2Si_{1-x}Sn_x$ ($0 \leq x \leq 1.0$) solid solutions by microwave irradiation," *Adv. Mater. Res.*, vol. 197, pp. 417–420, Feb. 2011.

[15] Z. Fan, M. D. Cappelluti, and D. H. Gregory, "Ultrafast, energy-efficient synthesis of intermetallics; microwave-induced metal plasma (MIMP) synthesis of Mg_2Sn," *ACS Sustain. Chem. Eng.*, vol. 7, no. 24, pp. 19686–19698, Nov. 2019.

[16] S. K. Bux, M. T. Yeung, E. S. Toberer, G. J. Snyder, R. B. Kaner, and J. P. Fleurial, "Mechanochemical synthesis and thermoelectric properties of high quality magnesium silicide," *J. Mater. Chem.*, vol. 21, no. 33, pp. 12259–12266, Sep. 2011.

[17] J. She, F. S. Pan, H. H. Hu, A. T. Tang, Z. W. Yu, and K. Song, "Effect of Mg_2Sn intermetallic on the grain refinement in As-cast AM series alloy," *J. Mater. Eng. Perform.*, vol. 24, no. 8, pp. 2937–2943, Aug. 2015.

[18] C. Fang, Z. Wen, X. Liu, H. Hao, G. Chen, and X. Zhang, "Microstructures and mechanical properties of Mg_2Sn-nanophase reinforced Mg–Mg_2Sn composite," *Mater. Sci. Eng. A*, vol. 684, pp. 229–232, Jan. 2017.

[19] V. Kevorkijan and S. Škapin, "Synthesis and characterisation of various Mg_2Sn-based composites made from laboratory prepared Mg_2Sn powder," *Mater. Manuf. Processes*, vol. 26, no. 4, pp. 623–631, Apr. 2011.

[20] Y.-F. Wu, W.-B. Du, and T.-Y. Zuo, "Synthesis kinetics of Mg_2Sn in Mg-Sn powder mixture using non-isothermal differential scanning calorimetry," *Trans. Nonferrous Met. Soc. China*, vol. 19, no. 5, pp. 1196–1200, Oct. 2009.

[21] M. Safavi, N. Martin, V. Linseis, F. Palmino, F. Cherioux, A. Billard, and M. A. P. Yazdi, "Thermoelectric properties improvement in Mg_2Sn thin films by structural modification," *J. Alloy. Compounds*, vol. 797, pp. 1078–1085, Aug. 2019.

[22] I. H. Jung, D. H. Kang, W. J. Park, N. J. Kim, and S. Ahn, "Thermodynamic modeling of the Mg–Si–Sn system," *Calphad*, vol. 31, no. 2, pp. 192–200, Jun. 2007.

[23] Z. Moser, W. Zakulski, Z. Panek, M. Kucharski, and L. Zabdyr, "Thermodynamic study and the phase diagram of the Mg-Sn system," *Metall. Trans. B*, vol. 21, no. 4, pp. 707–714, Aug. 1990.

[24] G.-H. Song, G.-P. Li, X.-Y. Li, H. Du, F. Hu, and L. Yin, "The microstructure and thermoelectric properties of the Mg_2(Sn,Si,Bi) films containing excess metal Mg phase," *Thin Solid Films*, vol. 713, Nov. 2020, Art. no. 138322.

[25] Q. Zhang, Q. Lu, Y. Yan, X. Su, and X. Tang, "Ultrafast synthesis and related phase evolution of Mg_2Si and Mg_2Sn compounds," *J. Electron. Mater.*, vol. 46, no. 5, pp. 3172–3181, May 2017.

[26] D. Larcher, A. S. Prakash, J. Saint, M. Morcrette, and J.-M. Tarascon, "Electrochemical reactivity of Mg_2Sn phases with metallic lithium," *Chem. Mater.*, vol. 16, no. 25, pp. 5502–5511, Dec. 2004.

[27] Y. Li, Y. Zhang, X. Kong, Y. Deng, R. Zhang, and J. Tang, "Investigation on thermodynatic performances of Mg_2Sn compound via first principle calculations," *Int. J. Heat Technol.*, vol. 34, no. 1, pp. 110–114, Mar. 2016.

[28] H. Sakaguchi, H. Maeta, M. Kubota, H. Honda, and T. Esaka, "Mg_2Sn as a new lithium storage intermetallic compound," *Electrochemistry*, vol. 68, no. 8, pp. 632–635, Aug. 2000.

[29] T.-H. An, C. Park, W.-S. Seo, S.-M. Choi, I.-H. Kim, and S.-U. Kim, "Enhancement of p-type thermoelectric properties in an Mg_2Sn system," *J. Korean Phys. Soc.*, vol. 60, no. 10, pp. 1717–1723, May 2012.

[30] S. W. Bae, S.-H. Kim, J. U. Lee, W.-K. Jo, W.-H. Hong, W. Kim, and S. H. Park, "Improvement of mechanical properties and reduction of yield asymmetry of extruded Mg-Al-Zn alloy through Sn addition," *J. Alloys Compounds*, vol. 766, pp. 748–758, Oct. 2018.

[31] F. Yu, J.-X. Sun, and T.-H. Chen, "High-pressure phase transitions of Mg_2Ge and Mg_2Sn: First-principles calculations," *Phys. B, Condens. Matter*, vol. 406, no. 9, pp. 1789–1794, Apr. 2011.

[32] O. Benhelal, A. Chahed, S. Laksari, B. Abbar, B. Bouhafs, and H. Aourag, "First-principles calculations of the structural, electronic and optical properties of IIA–IV antifluorite compounds," *Phys. Status Solidi B, Basic Res.*, vol. 242, no. 10, pp. 2022–2032, Aug. 2005.

[33] X. Liu, L. Xi, W. Qiu, J. Yang, T. Zhu, X. Zhao, and W. Zhang, "Significant roles of intrinsic point defects in $Mg_2X(X =$ Si, Ge, Sn) thermoelectric materials," *Adv. Electron. Mater.*, vol. 2, no. 2, Feb. 2016, Art. no. 1500284.

[34] S. Howlader, R. Vasudevan, B. Jarwal, S. Gupta, K.-H. Chen, K. Sachdev, and M. K. Banerjee, "Microstructure and mechanical stability of Bi doped $Mg_2Si_{0.4}Sn_{0.6}$ thermoelectric material," *J. Alloys Compounds*, vol. 818, Mar. 2020, Art. no. 152888.

[35] R. Lv, X. Guan, J. Zhang, Y. Xia, and J. Luo, "Enabling Mg metal anodes rechargeable in conventional electrolytes by fast ionic transport interphase," *Nat. Sci. Rev.*, vol. 7, no. 2, pp. 333–341, Feb. 2020.

[36] P. Claus, F. Raif, S. Cavet, S. Demirel-Gülen, J. Radnik, M. Schreyer, and T. Fässler, "From molecule to material: Mg_2Sn as hydrogenation catalyst," *Catal. Commun.*, vol. 7, no. 9, pp. 618–622, Sep. 2006.

[37] S. H. Kim, J.-P. Choi, Y.-S. Eom, Y. Nam, S. Baek, and C. Aranas, Jr., "A phenomenological study of a Sn–Ag–Al composite solder reinforced with Mg–MWCNT: Improved electrical conductivity and thermo-physical performance," *Mater. Des.*, vol. 140, pp. 196–208, Feb. 2018.

[38] T. Zhou, W. K. Pang, C. Zhang, J. Yang, Z. Chen, H. K. Liu, and Z. Guo, "Enhanced sodium-ion battery performance by structural phase transition from two-dimensional hexagonal-SnS_2 to orthorhombic-SnS," *ACS Nano*, vol. 8, no. 8, pp. 8323–8333, Aug. 2014.

[39] J. Grigas, E. Talik, and V. Lazauskas, "X-ray photoelectron spectra and electronic structure of Bi_2S_3 crystals," *Phys. Status Solidi B, Basic Res.*, vol. 232, no. 2, pp. 220–230, Aug. 2002.

[40] Y. M. Vysochanskii, D. Baltrunas, A. A. Grabar, K. Mazeika, K. Fedyo, and A. Sudavicius, "Mössbauer ^{119}Sn and XPS spectroscopy of $Sn_2P_2S_6$ and SnP_2S_6 crystals," *Phys. Status Solidi B, Basic Res.*, vol. 246, no. 5, pp. 1110–1117, May 2009.

[41] G. A. Samara, "Pressure and temperature dependences of the ionic conductivities of cubic and orthorhombic lead fluoride (PbF_2)," *J. Phys. Chem. Solids*, vol. 40, no. 7, pp. 509–522, 1979.

[42] S. Singh, M. Zeeshan, U. Singh, J. van den Brink, and H. C. Kandpal, "First-principles investigations of orthorhombic-cubic phase transition and its effect on thermoelectric properties in cobalt-based ternary alloys," *J. Phys., Condens. Matter*, vol. 32, no. 5, Nov. 2019, Art. no. 055505.

[43] S. Ohno, K. Imasato, S. Anand, H. Tamaki, S. D. Kang, P. Gorai, H. K. Sato, E. S. Toberer, T. Kanno, and G. J. Snyder, "Phase boundary mapping to obtain n-type Mg_3Sb_2-based thermoelectrics," *Joule*, vol. 2, no. 1, pp. 141–154, Jan. 2018.

[44] A. Dobrovolsky, A. Merdasa, E. L. Unger, A. Yartsev, and I. G. Scheblykin, "Defect-induced local variation of crystal phase transition temperature in metal-halide perovskites," *Nature Commun.*, vol. 8, no. 1, pp. 1–8, Jun. 2017.

[45] A. P. Levanyuk and A. S. Sigov, "Influence of defects on structural phase transitions," *Ferroelectrics*, vol. 63, no. 1, pp. 39–48, Jun. 1985.

[46] T. Vojta, "Smearing of the phase transition in Ising systems with planar defects," *J. Phys. A, Math. Gen.*, vol. 36, no. 43, Oct. 2003, Art. no. 10921.

[47] B. Ryu, E.-A. Choi, S. Park, J. Chung, J. de Boor, P. Ziolkowski, E. Müller, and S. Park, "Native point defects and low p-doping efficiency in Mg_2(Si,Sn) solid solutions: A hybrid-density functional study," *J. Alloys Compounds*, vol. 853, Feb. 2021, Art. no. 157145.

[48] W. Saito, K. Hayashi, J. Dong, J.-F. Li, and Y. Miyazaki, "Control of the thermoelectric properties of Mg_2Sn single crystals via point-defect engineering," *Sci. Rep.*, vol. 10, no. 1, pp. 1–9, Dec. 2020.

[49] K. Hayashi, Y. Miyazaki, W. Saito, M. Kubouchi, Y. Ogawa, S. Suzuki, Y. Hayashibara, and I. Ando, "Thermoelectric properties of Mg_2Si and its derivatives: Effects of lattice defects and secondary phases," in *Thermoelectric Materials: Principles and Concepts for Enhanced Properties*, 1st ed. Boston, MA, USA: De Gruyter, 2020, pp. 99–116. [Online]. Available: https://www.degruyter.com/document/doi/10.1515/9783110596526/pdf

[50] Z. Wu, Z. Luo, Y. Shen, W. Zhao, W. Wang, H. Nan, X. Guo, L. Sun, X. Wang, Y. You, and Z. Ni, "Defects as a factor limiting carrier mobility in WSe_2: A spectroscopic investigation," *Nano Res.*, vol. 9, no. 12, pp. 3622–3631, Dec. 2016.

[51] M. Jiang, H. Xiao, S. Peng, L. Qiao, G. Yang, Z. Liu, and X. Zu, "First-principles study of point defects in GaAs/AlAs superlattice: The phase stability and the effects on the band structure and carrier mobility," *Nanosc. Res. Lett.*, vol. 13, no. 1, pp. 1–3, Dec. 2018.

[52] E. S. Parrott, R. L. Milot, T. Stergiopoulos, H. J. Snaith, M. B. Johnston, and L. M. Herz, "Effect of structural phase transition on charge-carrier lifetimes and defects in $CH_3NH_3SnI_3$ perovskite," *J. Phys. Chem. Lett.*, vol. 7, no. 7, pp. 1321–1326, Apr. 2016.

[53] S. Guo, "First-principles calculations of Mg_2X ($X =$ Si, Ge, Sn) semiconductors with the calcium fluorite structure," *J. Semicond.*, vol. 36, no. 5, May 2015, Art. no. 053002.

[54] M. Guezlane, H. Baaziz, Z. Charifi, A. Belgacem-Bouzida, and Y. Djaballah, "A study of the phase transitions, electronic structures and thermodynamic properties of Mg_2X ($X =$ Ge, Si and Sn) under high pressure," *J. Sci., Adv. Mater. Devices*, vol. 2, no. 1, pp. 105–114, Mar. 2017.

[55] D. Errandonea, C. Popescu, A. B. Garg, P. Botella, D. Martinez-García, J. Pellicer-Porres, P. Rodríguez-Hernández, A. Muñoz, V. Cuenca-Gotor, and J. A. Sans, "Pressure-induced phase transition and band-gap collapse in the wide-band-gap semiconductor $InTaO_4$," *Phys. Rev. B, Condens. Matter*, vol. 93, no. 3, Jan. 2016, Art. no. 035204.

[56] Z. A. A. R. Almaghbash, O. Arbouche, A. Cherifi, S. Kessair, A. Zenati, and Y. Azzaz, "Enhanced thermoelectric performances driven by high-pressure phase transition of Mg_2Sn compound," *Int. J. Thermophys.*, vol. 41, no. 9, pp. 1–4, Sep. 2020.

[57] M. L. Cohen, "Superconductivity in many-valley semiconductors and in semimetals," *Phys. Rev.*, vol. 134, no. 2, pp. A511–A521, Apr. 1964.

[58] J. Xin, Y. Tang, Y. Liu, X. Zhao, H. Pan, and T. Zhu, "Valleytronics in thermoelectric materials," *NPJ Quantum Mater.*, vol. 3, no. 1, pp. 1–10, Feb. 2018.

[59] Y. Imai, M. Mukaida, and T. Tsunoda, "Calculation of electronic energy and density of state of iron-disilicides using a total-energy pseudopotential method, CASTEP," *Thin Solid Films*, vol. 381, no. 2, pp. 176–182, Jan. 2001.

[60] B. R. Rano, I. M. Syed, and S. H. Naqib, "Elastic, electronic, bonding, and optical properties of WTe_2 Weyl semimetal: A comparative investigation with $MoTe_2$ from first principles," *Results Phys.*, vol. 19, Dec. 2020, Art. no. 103639.

[61] D. Byeon, R. Sobota, K. Delime-Codrin, S. Choi, K. Hirata, M. Adachi, M. Kiyama, T. Matsuura, Y. Yamamoto, M. Matsunami, and T. Takeuchi, ''Discovery of colossal Seebeck effect in metallic Cu_2Se,'' *Nature Commun.*, vol. 10, no. 1, pp. 1–7, Jan. 2019.
[62] G. S. Nolas, H. Takizawa, T. Endo, H. Sellinschegg, and D. C. Johnson, ''Thermoelectric properties of Sn-filled skutterudites,'' *Appl. Phys. Lett.*, vol. 77, no. 1, pp. 52–54, Jul. 2000.
[63] A. Kumar, D. Sivaprahasam, and A. D. Thakur, ''Colossal Seebeck coefficient in Aurivillius phase-perovskite oxide composite,'' *J. Alloys Compounds*, vol. 853, Feb. 2021, Art. no. 157001.
[64] M. Battiato, J. M. Tomczak, Z. Zhong, and K. Held, ''Unified picture for the colossal thermopower compound $FeSb_2$,'' *Phys. Rev. Lett.*, vol. 114, no. 23, Jun. 2015, Art. no. 236603.
[65] P. Pichanusakorn and P. Bandaru, ''Nanostructured thermoelectrics,'' *Mater. Sci. Eng. R, Rep.*, vol. 67, nos. 2–4, pp. 19–63, Jan. 2010.
[66] K. B. Masood, P. Kumar, R. A. Singh, and J. Singh, ''Odyssey of thermoelectric materials: Foundation of the complex structure,'' *J. Phys. Commun.*, vol. 2, no. 6, Jun. 2018, Art. no. 062001.

SARA KIM received the B.S. degree in computer and electrical engineering from Tehran University, Tehran, Iran, in 2006, and the M.S. degree in electrical and electronic engineering from Yonsei University, Seoul, South Korea, in 2015. She is currently pursuing the Ph.D. degree with the Department of Electrical Engineering, Chosun University, Gwangju, South Korea. From 2006 to 2019, she was an Electrical Engineer/a Researcher at several companies. Her current research interest is semiconductor materials and devices.

NAM-HOON KIM received the B.S., M.S., and Ph.D. degrees in electrical engineering from Chung-Ang University, Seoul, South Korea, in 1997, 1999, and 2004, respectively. He continued his research as a Research Professor at Chosun University, Gwangju, South Korea, Sungkyunkwan University, and Chonnam National University, South Korea, from 2004 to 2010. In 2010, he joined the faculty with the Department of Electrical Engineering, Chosun University, where he is currently an Associate Professor. He is the author of more than 95 international journal articles. His research interests include electronic devices and semiconductor process, electrical materials and material characteristics, photovoltaic materials and solar cells, functional materials for energy devices, and nanoscience and nanotechnology.